Chemical Science

ROYAL SOCIETY OF CHEMISTRY

EDGE ARTICLE

View Article Online
View Journal | View Issue

Check for updates

Cite this: *Chem. Sci.*, 2024, **15**, 1782

All publication charges for this article have been paid for by the Royal Society of Chemistry

Received 13th October 2023
Accepted 21st December 2023

DOI: 10.1039/d3sc05434a

rsc.li/chemical-science

Significant hydrogen generation *via* photo-mechanical coupling in flexible methylammonium lead iodide nanowires†

Yucheng Zhang,[a] Jiawei Huang,[a] Mengya Zhu,[b] Zhouyang Zhang,[b] Kaiqi Nie,[c] Zhiguo Wang,[a] Xiaxia Liao,[a] Longlong Shu,[a] Tingfang Tian,*[a] Zhao Wang,*[d] Yang Lu[e] and Linfeng Fei*[a]

The flexoelectric effect, which refers to the mechanical-electric coupling between strain gradient and charge polarization, should be considered for use in charge production for catalytically driving chemical reactions. We have previously revealed that halide perovskites can generate orders of higher magnitude flexoelectricity under the illumination of light than in the dark. In this study, we report the catalytic hydrogen production by photo-mechanical coupling involving the photoflexoelectric effect of flexible methylammonium lead iodide ($MAPbI_3$) nanowires (NWs) in hydrogen iodide solution. Upon concurrent light illumination and mechanical vibration, large strain gradients were introduced in flexible $MAPbI_3$ NWs, which subsequently induced significant hydrogen generation (at a rate of 756.5 μmol g^{-1} h^{-1}, surpassing those values from either photo- or piezocatalysis of $MAPbI_3$ nanoparticles). This photo-mechanical coupling strategy of mechanocatalysis, which enables the simultaneous utilization of multiple energy sources, provides a potentially new mechanism in mechanochemistry for highly efficient hydrogen production.

Introduction

Mechanocatalysis, which triggers chemical reactions by mechanical deformation-induced charge energetics and separation, is an emerging field of advanced catalysis due to its unique potential to achieve the direct conversion of mechanical energy into chemical energy.[1] For instance, piezocatalysis, a typical mechanocatalysis, promotes redox reactions directly by mechanical stimuli-induced polarization charges (piezoelectric effect, *i.e.*, the coupling between strain and polarization charges) and the subsequent physical or chemical electron transfer.[2] Principally, piezocatalysts with high piezoelectric coefficients and substantial stresses are advantageous for achieving effective piezoelectric charge polarization. Therefore, the low-dimensional piezocatalysts[3–5] integrated with the piezoelectric effect and semiconductor properties (where the small size or dimensionality-reduced shape of nanomaterials allows large lattice strain and hence enhanced piezoelectricity)[6–8] are highly appealing. These materials are not only attractive for exploring new physical phenomena at the nanoscale, but also potentially capable of driving redox reactions with the assistance of environmental vibrations (waves, wind, *etc.*).[9,10] In this context, there has been a remarkable increase in the studies of piezocatalysis for nanoscale semiconductors in a range of applications, such as dye degradation,[11] hydrogen production, CO_2 reduction,[12] tooth whitening,[13] tumor therapy,[14] and organic synthesis.[15]

Piezoelectric-induced charge separation occurs when non-centrosymmetric materials are deformed by external stress.[16,17] However, upon exposure to random external stresses, internal strain gradients are inevitably introduced in materials, besides the existence of strain.[18,19] This has drawn attention to another ubiquitous electromechanical coupling effect, which is the flexoelectric effect.[20] Flexoelectricity refers to the electromechanical coupling between strain gradient and polarization,[21] which could induce piezoelectric-like polarization charges; this phenomenon widely exists in insulators, liquid crystals, biological samples, and semiconductors[22] (whereas piezoelectric materials must be in non-centrosymmetric crystals). In bulk materials, the flexoelectric effect is sometimes negligible due to the small strain gradient within the fracture limitation, but it becomes more significant when the crystal size is shrunk down

---

[a] School of Physics and Materials Science, Nanchang University, Nanchang 330031, China. E-mail: feilinfeng@gmail.com; tftian@ncu.edu.cn

[b] Department of Mechanical Engineering, City University of Hong Kong, Kowloon, Hong Kong SAR, China

[c] Institute of High Energy Physics, Chinese Academy of Sciences, Beijing 100049, China

[d] Hubei Key Laboratory of Micro- & Nano electronic Materials and Devices, School of Microelectronics, Hubei University, Wuhan 430062, China. E-mail: wangzhao@hubu.edu.cn

[e] Department of Mechanical Engineering, The University of Hong Kong, Hong Kong SAR, China

† Electronic supplementary information (ESI) available. See DOI: https://doi.org/10.1039/d3sc05434a

to the nanoscale.[23–25] It is noted that a few studies on flexocatalysis of nanomaterials have been reported, mainly focusing on the applications of dye degradation. Zhonglin Wang *et al.* suggested that under ultrasonic excitation, reactive species were created due to strain-gradient-induced flexoelectric polarization in MnO_2 nanosheets composed of nanoflowers, which could be used to degrade organic pollutants, such as methylene blue.[26] Yaojin Wang *et al.* also demonstrated the flexocatalysis effect in centrosymmetric $SrTiO_3$ nanoparticles for degrading organic dyes (rhodamine B).[27]

Inspiringly, in our recent work, we have demonstrated that the flexoelectricity in halide perovskites can be significantly enhanced upon the illumination of light, where the materials deliver orders of higher magnitude flexoelectric responses than normal bending-induced flexoelectricity.[28] This giant photoflexoelectric effect provides a whole new paradigm for harvesting multiple forms of energy at the same time. Although these halide perovskite materials are well known to suffer severe decomposition in aqueous solutions,[29,30] their dynamic equilibrium of dissolution and precipitation in solution can still enable photocatalytic hydrogen iodide (HI) decomposition together with hydrogen (H_2) generation.[31] For example, Yang Chai *et al.* have recently evidenced that methylammonium lead iodide ($MAPbI_3$) powder exhibited excellent piezoelectric photocatalytic hydrogen production efficiency in HI aqueous solution.[32]

Herein, we report the first case of catalytic hydrogen production by photo-mechanical coupling involving the photoflexoelectric effect from flexible $MAPbI_3$ nanowires (NWs) in HI solution. It is worth noting that NWs with a large aspect ratio were used as catalysts in this study because they can generate significant flexoelectricity by experiencing a large strain gradient (see discussions below). The photo-enhanced electromechanical coupling in $MAPbI_3$ NWs achieved a significant hydrogen production rate of 756.5 μmol g^{-1} h^{-1} by catalytic decomposition of HI, which is much higher than the reported values from similar systems *via* photo- or photopiezocatalysis. The development of this photo-mechanical coupling strategy in mechanocatalysis provides a potential "shortcut" in simultaneous utilization of multiple energy sources, which may shed light on new mechanisms for efficient mechanocatalysis.

Results and discussion

We synthesized $MAPbI_3$ NWs according to the widely reported wet-chemical method.[33] $MAPbI_3$ nanoparticles (NPs) and single crystals (SCs) were also synthesized for comparison purposes (see Methods for details). Systematical characterizations were first performed to check the structural information of the as-synthesized samples. Fig. 1a shows the scanning electron microscopy (SEM) image of a crowd of NWs, revealing their typical one-dimensional structures as well as the smooth surfaces (with average diameters of 360 nm and lengths up to 37 μm; see statistical results of their diameters and lengths in Fig. S1†). The transmission electron microscopy (TEM) image in Fig. 1b further demonstrates the smooth surface of a NW. Fig. 1c–e present the energy dispersive spectroscopy (EDS) elemental mappings for Pb, I, and N within a selected NW; the synchronous distributions of these constituent elements imply its uniform composition (one more set of data can be found in Fig. S2†). The selected area electron diffraction (SAED) pattern from an isolated NW in Fig. 1f confirms its single crystalline nature, and the pattern was assigned to a tetragonal structure as reported in previous syntheses.[34,35] Furthermore, the high-resolution TEM (HRTEM) image (Fig. 1g) exhibits distinct lattice fringes with a pair of interplanar spacings of 0.399 and 0.366 nm, corresponding to the (−103) and (202) planes of tetragonal $MAPbI_3$, respectively. In addition, the X-ray diffraction (XRD) patterns of $MAPbI_3$ SC, NPs, and NWs (Fig. 1h) show that the diffraction peaks at 14.29° and 28.62° correspond well to the (110) and (220) planes of tetragonal $MAPbI_3$, indicating their preferential orientation along [110] directions.[36] The minor existence of PbI_2 (refer to the low-intensity peaks at $2\theta = 12.84°$, 26.09°, 34.46°, and 39.69°) is common in these nanomaterials.[37]

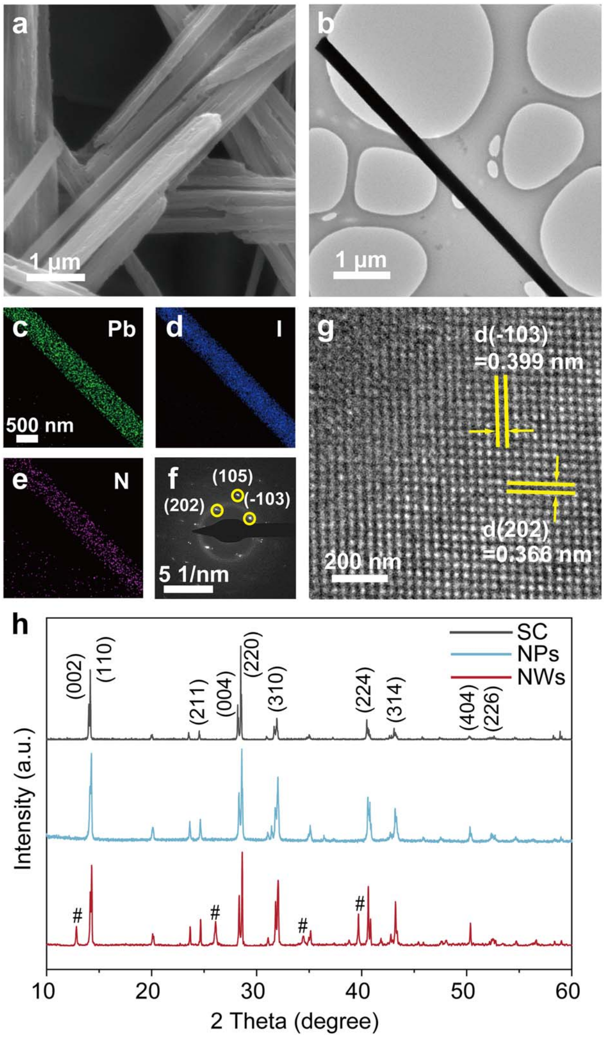

Fig. 1 Structural characterizations for $MAPbI_3$ NWs. (a) SEM image. (b) Bright-field TEM image. (c–e) EDS elemental mappings for Pb, I, and N on a NW. (f) SAED pattern. (g) Lattice-resolved HRTEM image. (h) XRD patterns for three $MAPbI_3$ samples.

The generation and separation of charge carriers, as well as their subsequent migration into the reaction systems, play a crucial role in the catalytic performance of catalysts. Ultraviolet photoelectron spectroscopy (UPS) and ultraviolet-visible (UV-Vis) absorption spectroscopy were undertaken to construct the band diagram of $MAPbI_3$ NWs. As shown in Fig. 2a, the as-synthesized $MAPbI_3$ NWs exhibit a maximum binding energy of 1.21 eV. The respective valence band positions of the NPs and SC samples were also assessed (Fig. S3†) and are consistent with the recent reports.[38,39] The UV-Vis spectra (Fig. 2b) reveal pronounced light absorption within the three samples. The samples present their sharp absorption edges in the infrared region, which signifies that electrons within the samples undergo efficient transitions from the valence band to the conduction band under the irradiation of visible light. The superior light absorption of NWs as compared to NPs and SC, which was possibly caused by the large surface area and the low stacking density of NWs,[40,41] implies the higher efficiency of the generation of the energetic electron–hole pairs. Fig. 2c presents the Tauc plot for the optical bandgap calculation of $MAPbI_3$ NWs, which is 1.54 eV (the corresponding values for the SC and NP samples are 1.51 and 1.54 eV, respectively; see Fig. S4,† as well as the comparison of the structures for optical bandgaps of $MAPbI_3$ SC, NWs, and NPs in Fig. S5†). The band diagram of the $MAPbI_3$ NWs revealed that its conduction band minimum (CBM) and valence band maximum (VBM) corresponded to −0.63 and 0.91 V *versus* the normal hydrogen electrode (NHE), respectively. These energy positions are well-suited for hydrogen reduction (0.046 V *versus* NHE) and iodine oxidation (0.376 V *versus* NHE) within our saturated HI aqueous system, as depicted in the inset of Fig. 2c. Therefore, during the catalytic process, the holes from the VBM exhibit stronger oxidation capability compared to I^- ions, leading to the oxidation of I^- ions to I_3^- ions, while the electrons from the CBM are more reducible than H^+, resulting in the reduction of H^+ to form H_2 (*i.e.*, $3I^- + 2h^+ = I_3^-$, $2H^+ + 2e^- = H_2$).

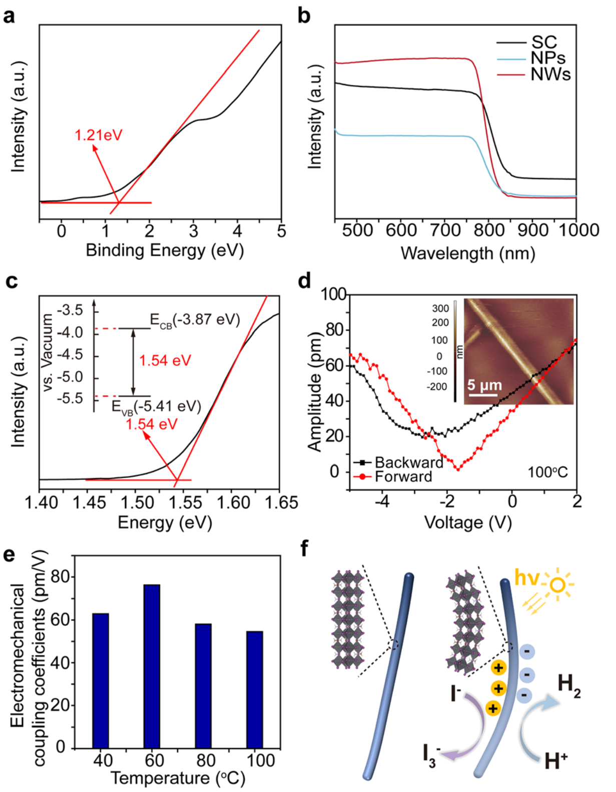

Fig. 2 Optical and electrical characterizations for $MAPbI_3$ NWs. (a) UPS spectrum for $MAPbI_3$ NWs. (b) UV-Vis absorption spectra for $MAPbI_3$ SC, NPs, and NWs. (c) Tauc plot for $MAPbI_3$ NWs; inset is the schematic diagram for the optical bandgap of $MAPbI_3$ NWs. (d) PFM response for an $MAPbI_3$ NW at 100 °C (inset: the corresponding PFM image). (e) Temperature-dependent electromechanical coupling coefficients for NWs. (f) Schematic illustration for the charge production induced by photo-mechanical coupling in $MAPbI_3$ NWs.

We then utilized the piezoelectric response force microscopy (PFM) mode of a scanning probe microscope (SPM) to assess the electromechanical coupling behavior of a single $MAPbI_3$ NW.[42] As shown in Fig. 2d, the applied voltage through the PFM tip indeed induced the mechanical response of the underlying NW, which confirms the electromechanical coupling in the $MAPbI_3$ NW. Furthermore, as the Curie temperature (*i.e.*, the piezoresponse should become zero above this temperature) of $MAPbI_3$ material is around 60 °C,[43] we also tested *in situ* the PFM response of NWs at a temperature range across its Curie temperature to verify the origin of the electromechanical coupling (Fig. S6 and S7†). The disappearance of hysteresis in the phase-voltage curves above the Curie temperature confirms the ferroelectric to non-ferroelectric transition for the NW (Fig. S7†). However, as it can be seen in Fig. 2e, the electromechanical coupling coefficient was maintained within 76 to 54 pm V^{-1} (the system has been calibrated by a standard $LiNbO_3$ sample with its d_{33} of 17.3 pm V^{-1}; see Fig. S8†), which indicated that the NW retained more than 70% of the electromechanical coupling response despite the absence of piezoelectric effect at the temperature beyond Curie point; in brief, it is confirmed that the as-measured electromechanical coupling of $MAPbI_3$ NWs was mainly attributed to the flexoelectric effect.

Furthermore, perovskite bulk materials are well known to be extremely fragile, which would be a significant issue for their applications in mechanocatalysis (in which large deformations of materials are essential for charge generation). However, when the dimensions of a sample are reduced toward the nanoscale, they may manifest exceptional flexibility, enabling them to withstand intense mechanical forces such as ultrasonication and stirring without being damaged. In the SEM/TEM observations, we observed a few bending NWs (see Fig. S9† for a representative example), which inspired the high flexibility of these $MAPbI_3$ NWs. Consequently, *in situ* experiments were conducted to observe the bending behaviors of $MAPbI_3$ NWs (the setup is schematically shown in Fig. 3a; see Methods for details). Upon forced bending by a rigid needle at one end, a single NW endured a large curvature (defined as how much the curve deviates from a straight line) before it was broken; yet under controlled deflection, the NW can be cycled between bending and straight states (as shown in Fig. 3b and c; the K values denoted on panels show the corresponding curvatures). During multiple bending processes, it was observed that the

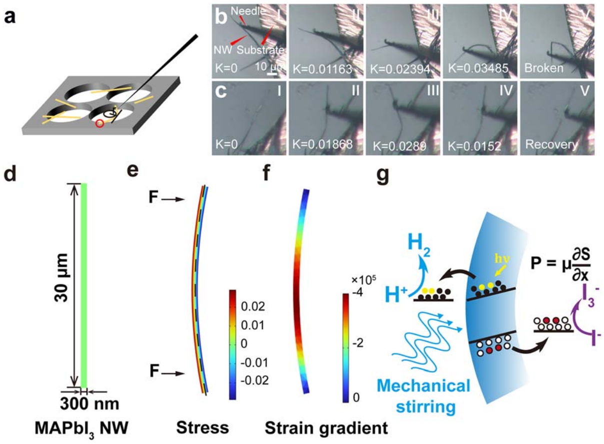

Fig. 3 Bending behaviors of $MAPbI_3$ NWs. (a) Schematic diagram for the *in situ* bending test of a single $MAPbI_3$ NW. (b) *In situ* bending of an $MAPbI_3$ NW until broken. (c) *In situ* bending of an $MAPbI_3$ NW and its recovery. (d) A single NW model for FEM. (e) FEM results for bending-induced stress distribution within a single NW. (f) FEM distributions of bending-induced strain gradient within the NW. (g) Schematic illustration for the photo-mechanical coupling in a bending $MAPbI_3$ NW.

NW exhibited excellent flexibility (Fig. S10; also refer to the ESI Movie†), which is suitable for repeated bending-recovery cycles in mechanocatalysis.

Moreover, finite element method (FEM) simulations were employed to survey the bending-induced strain gradient within a single NW. For a model of $MAPbI_3$ NW, the length is set to 30 μm, and the diameter is set to 300 nm (Fig. 3d). The stress distribution (ε_{11}) within the $MAPbI_3$ NW upon experiencing bending moments at both ends is shown in Fig. 3e, in which one side (the red area) of the NW undergoes tensile stress, while the opposite side (the blue area) experiences compressive stress (the dashed line indicates the neutral plane, where $\varepsilon = 0$). Correspondingly, the strain progressively increases from the center towards the surface, while it decreases from the center to both ends of the NW along the axial direction. The strain gradient, however, manifests distinct variations across the NW due to the structural characteristics of this simply supported NW (Fig. 3f). One can see that the strain gradients at both ends of the NW are relatively low, whereas in the central region, there is significant augmentation in strain gradient (up to 10^5). This observation demonstrates that the morphology of NW facilitates the formation of strain gradients, subsequently giving rise to significant mechanoelectrical coupling for NWs. The polarization induced by this strain gradient would generate an electric field (E) perpendicular to the radial direction within the $MAPbI_3$ NW, together with the net charges at both surfaces. In our previous work, we obtained a flexoelectric coefficient of $\sim$2000 μC m^{-1} for halide perovskites;[28] as a result, a polarization strength of about 200 C m^{-2} in the $MAPbI_3$ NW can be calculated. This significant internal polarization could lead to a completely tilted band structure for $MAPbI_3$ material and drive the efficient dissociation of charge carriers, facilitating electrons and holes to be separated in opposite directions. When $MAPbI_3$ NWs are subjected to a varying field of external mechanical stimulations (*i.e.*, magnetic stirring), the repeated bending and recovery cycles of NWs would drive the random changes in their internal electrical fields (both strengths and directions), which induce the inclinations of the energy levels of NWS and continuous accumulation of charges (which was initiated by photo-induced separation) for catalysis (*i.e.*, photo-mechanocatalysis).[44] In this case, H^+ readily combines with the accumulated charges to produce H_2 (Fig. 3g).

It is therefore expected that the proposed photo-mechanical coupling in $MAPbI_3$ NWs should deliver significant catalytic performance. Consequently, we evaluated the catalytic performance of $MAPbI_3$ NWs in a $MAPbI_3$-saturated HI solution (though not in water because the material is soluble in water, with a solubility of 0.645 mol L^{-1} at 20 °C (ref. 31)) under simultaneous light illumination and mechanical stirring (see Methods). The as-synthesized $MAPbI_3$ NWs were added into a homemade quartz vessel filled with $MAPbI_3$-saturated HI solution, which was hermetically sealed and equipped with a magnetic agitator to induce mechanical stimulation along with a xenon lamp for illumination. Gas chromatography (GC) was employed to monitor the H_2 production from the reaction system. As anticipated, a substantial quantity of H_2 was produced by the photo-mechanocatalytic HI splitting induced by the flexible $MAPbI_3$ NWs. The results are illustrated in Fig. 4a, which was juxtaposed with the results obtained solely through photocatalysis and mechanocatalysis of the NWs (which were driven by either light or stirring, respectively). The hydrogen generation rates for photo-mechanocatalysis, mechanocatalysis, and photocatalysis were 756.5, 192.2, and 164.2 μmol g^{-1} h^{-1}, respectively; in other words, the amounts of H_2 generated by the photomechanocatalysis, mechanocatalysis, and photocatalysis in our experimental conditions were recorded as 75.65, 19.22, and 16.42 μmol in 2 hours, respectively (Fig. 4b; the original GC data can be referred to in Fig. S11 and S12†). It is thus evident that the hydrogen production *via* the photomechanocatalytic process is significantly higher than the combined hydrogen production from the mechanocatalytic and photocatalytic processes, which suggests a remarkable synergistic effect of photo-mechanical coupling on this system. Next, to verify the effect of $MAPbI_3$ morphology on the photo-mechanocatalytic performance, another group of control experiments was conducted by comparing the hydrogen generation rates of $MAPbI_3$ NWs and NPs, and the time-dependent hydrogen evolution profiles for $MAPbI_3$ NWs and NPs are shown in Fig. 4c. It is clear that the NWs exhibited a significantly higher hydrogen generation rate compared to the NPs (Fig. 4d), demonstrating the geometrical advantages of NWs in flexoelectric charge production,[45] as well as in photomechanocatalytic hydrogen production.

To mitigate the interference of hydrogen generation from the self-decomposition of HI under illumination and mechanical agitation, we replicated the previously mentioned experiment in the absence of $MAPbI_3$ NWs. No noticeable hydrogen evolution was detected in the scenarios involving sole illumination, sole agitation, or the combination of illumination and agitation (Fig. S13†). In this context, the hydrogen generation in previous experiments can be attributed to the photomechanocatalytic cleavage of HI induced by the $MAPbI_3$ NWs. To the best of our knowledge, the hydrogen production rate of $MAPbI_3$ NWs as reported in this work is one of the highest values for the single-

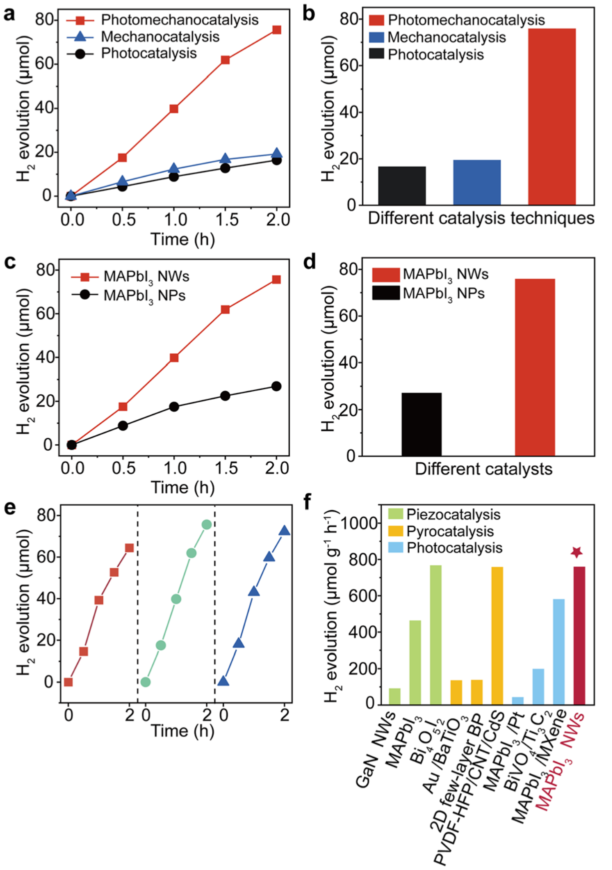

Fig. 4 Hydrogen production performances for MAPbI$_3$ NWs *via* photomechanocatalysis. (a) Time-dependent hydrogen evolution profiles for photomechanocatalysis, photocatalysis, and mechanocatalysis for MAPbI$_3$ NWs. (b) The comparative amounts of hydrogen generated from MAPbI$_3$ NWs after 2 h using different catalysis techniques. (c) Time-dependent hydrogen evolution profiles for MAPbI$_3$ NWs and NPs *via* photomechanocatalysis. (d) The comparative amounts of hydrogen generated from photomechanocatalysis after 2 h using MAPbI$_3$ NWs and NPs. (e) The test of stability for photomechanocatalytic hydrogen production using MAPbI$_3$ NWs over three cycles. (f) Comparison of hydrogen production rates among different catalytic modes and catalysts in recent reports. The listed examples include piezocatalysis (GaN NWs,[3] MAPbI$_3$,[32] Bi$_4$O$_5$I$_2$ (ref. 46)), pyrocatalysis (Au/BaTiO$_3$,[47] 2D few-layer black phosphorene,[48] PVDF-HFP/CNT/CdS[49]), photocatalysis (MAPbI$_3$/Pt,[50] BiVO$_4$/Ti$_3$C$_2$ nanosheets,[51] MAPbI$_3$/MXene[52]), and our work.

catalyst systems in HI (Table S1†). Moreover, the solar HI splitting efficiency of our experiment can reach up to 2.67% (the calculation can be found in Methods), which represents a significant improvement compared to the existing reports. Moreover, the cycling stability of MAPbI$_3$ NWs as catalysts in photomechanocatalytic hydrogen production was also assessed; as shown in Fig. 4e, the hydrogen production rates have been constantly maintained across three catalytic cycles, demonstrating the good repeatability of MAPbI$_3$ NWs in this catalytic reaction. In addition, a comprehensive analysis was conducted to investigate the microstructural evolution of MAPbI$_3$ NWs during the reaction process. The XRD spectrum of MAPbI$_3$ NWs after catalytic reaction is presented in Fig. S14.† Compared to the XRD pattern of NWs before the reaction (Fig. 1h), the peaks of MAPbI$_3$ remained essentially unchanged, indicating the NWs were basically stable in the catalytic system, while the peaks of PbI$_2$ disappeared as it dissolved in HI. Moreover, the NWs after different reaction times (0, 1, and 2 h) were isolated from the reaction system and further observed under SEM (Fig. S15†). In the prolonged reaction, the NWs exhibited slight surface damage due to mechanical stirring and possible photodegradation, yet the structure of the NWs was largely preserved. We further compared the hydrogen production rate in our experiment with the existing catalytic hydrogen generation approaches, including piezoelectric, pyroelectric, and photocatalytic pathways (as shown in Fig. 4f). The catalytic activity of MAPbI$_3$ NWs with photo-mechanical coupling exhibits a superior rate than, or at least, is comparable to a multitude of extensively investigated piezoelectric, pyroelectric, and photocatalytic systems.

Conclusions

In summary, an effective strategy for hydrogen production using flexible MAPbI$_3$ NWs upon concurrent light illumination and mechanical stirring was demonstrated with a hydrogen yield rate as high as 756.5 μmol g^{-1} h^{-1} (the corresponding catalytic efficiency is 2.67%), which surpasses the rates achieved by sole photocatalysis and flexocatalysis by nearly five-fold and four-fold, respectively. The significant photomechanocatalysis from MAPbI$_3$ NWs is attributed to the photo-mechanical coupling, which tilts the band structure of MAPbI$_3$ under large strain gradients and thus accelerates the charge production at the surfaces of NWs upon light illumination. Our work demonstrates the potential of MAPbI$_3$ NWs for hydrogen production *via* simultaneously harvesting mechanical and solar energy from the environment and may shed light on the paradigm shift in mechanocatalysis.

Data availability

The data that support the findings of this study are available from the corresponding authors upon reasonable request.

Author contributions

L.-F. F. conceived and supervised the project. L.-F. F. and Y.-C. Z. designed the experiments. J.-W. H. conducted TEM observations and data analysis. M.-Y. Z. and Z.-Y. Z. conducted the *in situ* bending test. K.-Q. N. and X.-X. L. conducted UPS measurements. Z.-G. W. performed FEM calculations. Y.-C. Z., T.-F. T., Z. W., and L.-F. F. wrote the manuscript with the help and input of all authors. All authors have given their approval to the final version of the manuscript.

Conflicts of interest

There are no conflicts to declare.

Acknowledgements

This work was jointly supported by the National Natural Science Foundation of China (51972159 and U21A20500) and Jiangxi Provincial Natural Science Foundation (20212ACB204016, 20192ACB21018, and 20171ACB20006). Y. L. acknowledges the support from the Hong Kong RGC General Research Fund (GRF) project (11200623). Z. W. acknowledges the support from the Hubei Provincial Natural Science Foundation (2023AFA074). L.-F. F. acknowledges the support from Nanchang University. The authors also acknowledge the use of the 4B9B beamline at the Beijing Synchrotron Radiation Facility.

References

1 L. Chen, Y. Yang, S. Jiang, B. Yang and W. Rao, Multifunctional ferroelectric catalysis for water splitting: classification, synergism, strategies and challenges, *Mater. Today Chem.*, 2023, **30**, 101486.

2 W. Qian, W. Yang, Y. Zhang, C. R. Bowen and Y. Yang, Piezoelectric materials for controlling electro-chemical processes, *Nano-Micro Lett.*, 2020, **12**, 149.

3 M. Zhang, S. Zhao, Z. Zhao, S. Li and F. Wang, Piezocatalytic effect induced hydrogen production from water over non-noble metal Ni deposited ultralong GaN nanowires, *ACS Appl. Mater. Interfaces*, 2021, **13**, 10916–10924.

4 Q. Nie, Y. Xie, J. Ma, J. Wang and G. Zhang, High piezo-catalytic activity of ZnO/Al_2O_3 nanosheets utilizing ultrasonic energy for wastewater treatment, *J. Cleaner Prod.*, 2020, **242**, 118532.

5 H. Lei, H. Zhang, Y. Zou, X. Dong, Y. Jia and F. Wang, Synergetic photocatalysis/piezocatalysis of bismuth oxybromide for degradation of organic pollutants, *J. Alloys Compd.*, 2019, **809**, 151840.

6 J. Yu, H. Guo, W. Feng, X. Guo, Y. Zhu, T. Thomas, C. Jiang, S. Liu and M. Yang, $Co_4N–WN_x$ composite for efficient piezocatalytic hydrogen evolution, *Dalton Trans.*, 2022, **51**, 7127–7134.

7 Q. Tang, J. Wu, D. Kim, C. Franco, A. Terzopoulou, A. Veciana, J. Puigmartí-Luis, X.-Z. Chen, B. J. Nelson and S. Pané, Enhanced piezocatalytic performance of $BaTiO_3$ nanosheets with highly exposed {001} facets, *Adv. Funct. Mater.*, 2022, **32**, 2202180.

8 S. Lin, S. Li, H. Huang, H. Yu and Y. Zhang, Synergetic piezo-photocatalytic hydrogen evolution on $Cd_xZn_{1-x}S$ solid-solution 1D nanorods, *Small*, 2022, **18**, 2106420.

9 C. Wang, C. Hu, F. Chen, T. Ma, Y. Zhang and H. Huang, Design strategies and effect comparisons toward efficient piezocatalytic system, *Nano Energy*, 2023, **107**, 108093.

10 S. Li, Z. Zhao, J. Zhao, Z. Zhang, X. Li and J. Zhang, Recent advances of ferro-, piezo-, and pyroelectric nanomaterials for catalytic applications, *ACS Appl. Nano Mater.*, 2020, **3**, 1063–1079.

11 H. You, X. Ma, Z. Wu, L. Fei, X. Chen, J. Yang, Y. Liu, Y. Jia, H. Li, F. Wang and H. Huang, Piezoelectrically/pyroelectrically-driven vibration/cold-hot energy harvesting for mechano-/pyro- bi-catalytic dye decomposition of $NaNbO_3$ nanofibers, *Nano Energy*, 2018, **52**, 351–359.

12 J. Ma, X. Xiong, D. Wu, Y. Wang, C. Ban, Y. Feng, J. Meng, X. Gao, J.-Y. Dai, G. Han, L.-Y. Gan and X. Zhou, Band position-independent piezo-electrocatalysis for ultrahigh CO_2 conversion, *Adv. Mater.*, 2023, **35**, 2300027.

13 Y. Wang, X. Wen, Y. Jia, M. Huang, F. Wang, X. Zhang, Y. Bai, G. Yuan and Y. Wang, Piezo-catalysis for nondestructive tooth whitening, *Nat. Commun.*, 2020, **11**, 1328.

14 P. Zhu, Y. Chen and J. Shi, Piezocatalytic tumor therapy by ultrasound-triggered and $BaTiO_3$-mediated piezoelectricity, *Adv. Mater.*, 2020, **32**, 2001976.

15 K. Kubota, Y. Pang, A. Miura and H. Ito, Redox reactions of small organic molecules using ball milling and piezoelectric materials, *Science*, 2019, **366**, 1500–1504.

16 S. Tu, Y. Guo, Y. Zhang, C. Hu, T. Zhang, T. Ma and H. Huang, Piezocatalysis and piezo-photocatalysis: Catalysts classification and modification strategy, reaction mechanism, and practical application, *Adv. Funct. Mater.*, 2020, **30**, 2005158.

17 J. Liu, W. Qi, M. Xu, T. Thomas, S. Liu and M. Yang, Piezocatalytic techniques in environmental remediation, *Angew. Chem., Int. Ed.*, 2023, **62**, 202213927.

18 P. Zubko, G. Catalan and A. K. Tagantsev, Flexoelectric effect in solids, *Annu. Rev. Mater. Res.*, 2013, **43**, 387–421.

19 T. D. Nguyen, S. Mao, Y.-W. Yeh, P. K. Purohit and M. C. McAlpine, Nanoscale flexoelectricity, *Adv. Mater.*, 2013, **25**, 946–974.

20 B. Wang, Y. Gu, S. Zhang and L.-Q. Chen, Flexoelectricity in solids: Progress, challenges, and perspectives, *Prog. Mater. Sci.*, 2019, **106**, 100570.

21 P. V. Yudin and A. K. Tagantsev, Fundamentals of flexoelectricity in solids, *Nanotechnology*, 2013, **24**, 432001.

22 J. Narvaez, F. Vasquez-Sancho and G. Catalan, Enhanced flexoelectric-like response in oxide semiconductors, *Nature*, 2016, **538**, 219–221.

23 L. Shu, R. Liang, Z. Rao, L. Fei, S. Ke and Y. Wang, Flexoelectric materials and their related applications: A focused review, *J. Adv. Ceram.*, 2019, **8**, 153–173.

24 Q. Deng, M. Kammoun, A. Erturk and P. Sharma, Nanoscale flexoelectric energy harvesting, *Int. J. Solids Struct.*, 2014, **51**, 3218–3225.

25 Z. Wang, C. Li, H. Xie, Z. Zhang, W. Huang, S. Ke and L. Shu, Effect of grain size on flexoelectricity, *Phys. Rev. Appl.*, 2022, **18**, 064017.

26 T. Wu, K. Liu, S. Liu, X. Feng, X. Wang, L. Wang, Y. Qin and Z. L. Wang, Highly efficient flexocatalysis of two-dimensional semiconductors, *Adv. Mater.*, 2023, **35**, 2208121.

27 Z. Liu, X. Wen, Y. Wang, Y. Jia, F. Wang, G. Yuan and Y. Wang, Robust flexo-catalysis in centrosymmetric nanoparticles, *Adv. Mater. Technol.*, 2022, **7**, 2101484.

28 L. Shu, S. Ke, L. Fei, W. Huang, Z. Wang, J. Gong, X. Jiang, L. Wang, F. Li, S. Lei, Z. Rao, Y. Zhou, R.-K. Zheng, X. Yao, Y. Wang, M. Stengel and G. Catalan, Photoflexoelectric effect in halide perovskites, *Nat. Mater.*, 2020, **19**, 605–609.

29 J. Zhao, B. Cai, Z. Luo, Y. Dong, Y. Zhang, H. Xu, B. Hong, Y. Yang, L. Li, W. Zhang and C. Gao, Investigation of the hydrolysis of perovskite organometallic halide $CH_3NH_3PbI_3$ in humidity environment, *Sci. Rep.*, 2016, **6**, 21976.

30 S. Chen, H. Yin, P. Liu, Y. Wang and H. Zhao, Stabilization and performance enhancement strategies for halide perovskite photocatalysts, *Adv. Mater.*, 2023, **35**, 2203836.

31 S. Park, W. J. Chang, C. W. Lee, S. Park, H.-Y. Ahn and K. T. Nam, Photocatalytic hydrogen generation from hydriodic acid using methylammonium lead iodide in dynamic equilibrium with aqueous solution, *Nat. Energy*, 2016, **2**, 16185.

32 M. Wang, Y. Zuo, J. Wang, Y. Wang, X. Shen, B. Qiu, L. Cai, F. Zhou, S. P. Lau and Y. Chai, Remarkably enhanced hydrogen generation of organolead halide perovskites *via* piezocatalysis and photocatalysis, *Adv. Energy Mater.*, 2019, **9**, 1901801.

33 Q. Ye, J. Zhang, P. Guo, H. Fan, D. G. Shchukin, B. Wei and H. Wang, Wet-chemical synthesis of surface-passivated halide perovskite microwires for improved optoelectronic performance and stability, *ACS Appl. Mater. Interfaces*, 2018, **10**, 43850–43856.

34 J. Xing, X. F. Liu, Q. Zhang, S. T. Ha, Y. W. Yuan, C. Shen, T. C. Sum and Q. Xiong, Vapor phase synthesis of organometal halide perovskite nanowires for tunable room-temperature nanolasers, *Nano Lett.*, 2015, **15**, 4571–4577.

35 P. Bansal and P. Kar, Ultralong micro-belts of luminescent lead halide-based perovskites, *Chem. Commun.*, 2019, **55**, 6543–6546.

36 X. Hu, X. Zhang, L. Liang, J. Bao, S. Li, W. Yang and Y. Xie, High-performance flexible broadband photodetector based on organolead halide perovskite, *Adv. Funct. Mater.*, 2014, **24**, 7373–7380.

37 N. Leupold, K. Schötz, S. Cacovich, I. Bauer, M. Schultz, M. Daubinger, L. Kaiser, A. Rebai, J. Rousset, A. Köhler, P. Schulz, R. Moos and F. Panzer, High versatility and stability of mechanochemically synthesized halide perovskite powders for optoelectronic devices, *ACS Appl. Mater. Interfaces*, 2019, **11**, 30259–30268.

38 M. Caputo, N. Cefarin, A. Radivo, N. Demitri, L. Gigli, J. R. Plaisier, M. Panighel, G. Di Santo, S. Moretti, A. Giglia, M. Polentarutti, F. De Angelis, E. Mosconi, P. Umari, M. Tormen and A. Goldoni, Electronic structure of $MAPbI_3$ and $MAPbCl_3$: importance of band alignment, *Sci. Rep.*, 2019, **9**, 15159.

39 P.-H. Chang, S.-Y. Liu, Y.-B. Lan, Y.-C. Tsai, X.-Q. You, C.-S. Li, K.-Y. Huang, A.-S. Chou, T.-C. Cheng, J.-K. Wang and C.-I. Wu, Ultrahigh responsivity and detectivity graphene–perovskite hybrid phototransistors by sequential vapor deposition, *Sci. Rep.*, 2017, **7**, 46281.

40 G. Zhou, L. Xu, G. Hu, L. Mai and Y. Cui, Nanowires for electrochemical energy storage, *Chem. Rev.*, 2019, **119**, 11042–11109.

41 S. Sofiane and M. Bilel, Effect of specific surface area on photoelectrochemical properties of TiO_2 nanotubes, nanosheets and nanowires coated with TiC thin films, *J. Photochem. Photobiol., A*, 2016, **324**, 126–133.

42 L. Fei, Y. Hu, X. Li, R. Song, L. Sun, H. Huang, H. Gu, H. L. W. Chan and Y. Wang, Electrospun bismuth ferrite nanofibers for potential applications in ferroelectric photovoltaic devices, *ACS Appl. Mater. Interfaces*, 2015, **7**, 3665–3670.

43 Y.-J. Kim, T.-V. Dang, H.-J. Choi, B.-J. Park, J.-H. Eom, H.-A. Song, D. Seol, Y. Kim, S.-H. Shin, J. Nah and S.-G. Yoon, Piezoelectric properties of $CH_3NH_3PbI_3$ perovskite thin films and their applications in piezoelectric generators, *J. Mater. Chem. A*, 2016, **4**, 756–763.

44 R. Su, J. Zhang, V. Wong, D. Zhang, Y. Yang, Z.-D. Luo, X. Wang, H. Wen, Y. Liu, J. Seidel, X. Yang, Y. Pan and F.-t. Li, Engineering sub-nanometer hafnia-based ferroelectrics to break the scaling relation for high-efficiency piezocatalytic water splitting, *Adv. Mater.*, 2023, **35**, 2303018.

45 X. Liang, S. Hu and S. Shen, Effects of surface and flexoelectricity on a piezoelectric nanobeam, *Smart Mater. Struct.*, 2014, **23**, 035020.

46 C. Wang, C. Hu, F. Chen, H. Li, Y. Zhang, T. Ma and H. Huang, Polar layered bismuth-rich oxyhalide piezoelectrics $Bi_4O_5X_2$ (X=Br, I): Efficient piezocatalytic pure water splitting and interlayer anion-dependent activity, *Adv. Funct. Mater.*, 2023, **33**, 2301144.

47 H. You, S. Li, Y. Fan, X. Guo, Z. Lin, R. Ding, X. Cheng, H. Zhang, T. W. B. Lo, J. Hao, Y. Zhu, H.-Y. Tam, D. Lei, C.-H. Lam and H. Huang, Accelerated pyro-catalytic hydrogen production enabled by plasmonic local heating of Au on pyroelectric $BaTiO_3$ nanoparticles, *Nat. Commun.*, 2022, **13**, 6144.

48 H. You, Y. Jia, Z. Wu, F. Wang, H. Huang and Y. Wang, Room-temperature pyro-catalytic hydrogen generation of 2D few-layer black phosphorene under cold-hot alternation, *Nat. Commun.*, 2018, **9**, 2889.

49 B. Dai, J. Fang, Y. Yu, M. Sun, H. Huang, C. Lu, J. Kou, Y. Zhao and Z. Xu, Construction of infrared-light-responsive photoinduced carriers driver for enhanced photocatalytic hydrogen evolution, *Adv. Mater.*, 2020, **32**, 1906361.

50 Y. Wu, P. Wang, X. Zhu, Q. Zhang, Z. Wang, Y. Liu, G. Zou, Y. Dai, M.-H. Whangbo and B. Huang, Composite of $CH_3NH_3PbI_3$ with reduced graphene oxide as a highly efficient and stable visible-light Photocatalyst for hydrogen evolution in aqueous HI solution, *Adv. Mater.*, 2018, **30**, 1704342.

51 Y. Li, Y. Liu, D. Xing, J. Wang, L. Zheng, Z. Wang, P. Wang, Z. Zheng, H. Cheng, Y. Dai and B. Huang, 2D/2D heterostructure of ultrathin $BiVO_4/Ti_3C_2$ nanosheets for photocatalytic overall water splitting, *Appl. Catal., B*, 2021, **285**, 119855.

52 W. Li, F. Wang, Z. Zhang and S. Min, $MAPbI_3$ microcrystals integrated with $Ti_3C_2T_x$ MXene nanosheets for efficient visible-light photocatalytic H_2 evolution, *Chem. Commun.*, 2021, **57**, 7774–7777.